Co(II), Ni(II), Cu(II), and Zn(II)-(*E*)-*N*'-(2-Hydroxybenzylidene)benzohydrazide Complexes: Design, Characterization, ADME Study, and Evaluation of Antibacterial Activity

Yusuf Syahril Alam, Nuraini Fitria, Amelia Bella Putri Adama, Shava Alifia Salsabilla, Shinta Ratna Duhita, Mardi Santoso, and Fahimah Martak*

Department of Chemistry, Faculty of Science and Data Analytics, Institut Teknologi Sepuluh Nopember, Jl. Arif Rahman Hakim, Surabaya 60115, Indonesia

* ***Corresponding author:***

tel: +62-81572535690
email: fahimahm@chem.its.ac.id

Received: December 2, 2024
Accepted: June 20, 2025

DOI: 10.22146/ijc.102090

Abstract: *Four new hydrazone complexes were successfully synthesized from Co(II), Ni(II), Cu(II), and Zn(II) metal ions with the ligand* (E)-N'-*(2-hydroxybenzylidene)benzohydrazide. Structural elucidation was performed using CHNSO elemental analysis, FTIR, UV-vis, thermal analysis, and powder XRD. The FTIR spectra indicated the presence of coordination bonds in the form of M–N and M–O. The UV-vis spectra showed LMCT transitions. TGA characterization revealed that the Co(II), Ni(II), and Cu(II) complexes have an M:L ratio of 1:1, whereas the Zn(II) complex has an M:L ratio of 1:2. These findings were corroborated by the refinement results of the experimental and standard XRD diffractogram. Accordingly, the formulas of the Co(II), Ni(II), Cu(II), and Zn(II) hydrazone complexes are* $[Co(L)(Cl)(H_2O)]$, $[Ni(L)(H_2O)_2]Cl_2$, $[Cu(L)(H_2O)]Cl$, *and* $[Zn(L)_2]$, *respectively. Furthermore, based on the determined M:L ratios, the Co(II), Ni(II), and Cu(II) complexes are inferred to possess square planar geometries, while the Zn(II) complex is suggested to be octahedral. The ADME study, aimed at assessing their potential as drug candidates, revealed various pharmacological characteristics of the compounds. Antibacterial evaluation against* Staphylococcus aureus *(G+) and* Escherichia coli *(G–) showed the Cu(II) complex with the highest activity.*

Keywords: *antibacterial; complexes;* (E)-N'-*(2-hydroxybenzylidene)benzohydrazide; hydrazone; ligand*

■ INTRODUCTION

Bacterial infections have become a serious threat to humans, marked by the emergence of various diseases and the deterioration of industrial supplies, food, and pharmaceuticals [1]. The adaptability of bacteria to novel and extreme environments allows them to proliferate rapidly within brief periods [2]. In healthcare, antibacterials are essential for suppressing and eradicating pathogenic bacteria [3]. Nevertheless, improper use or excessive dosing can contribute to the development of antibiotic resistance (ABR) [4]. Moreover, ABR can lead to death. In 2019, ABR was responsible for 1.27 million deaths, with *Escherichia coli* and *Staphylococcus aureus* being the leading contributors to these fatalities [5]. This underscores the urgent need for the development of new antibiotic agents.

Hydrazones are a class of organic compounds containing an azomethine group, formed by replacing the oxygen atom in aldehydes or ketones with a hydrazine nitrogen [6-7]. Derivatives of hydrazones have demonstrated efficacy across a range of bioactivities, such as antituberculosis [8], anticancer [9], antifungal [10], antioxidant [11], antidiabetic [12], antiviral [13], and antibacterial effects [14]. The carbon-nitrogen covalent bond within the azomethine group contributes to the formation of stable transition metal complexes [15]. Additionally, acyl group functionalization enhances the denticity of hydrazone metal complexes [16].

Hydrazone-based benzohydrazides (BZH) and their derivatives play a pivotal role in advancing a vital class of novel therapeutic agents. Prasanna and

Narender [17] synthesized benzoylhydrazones derived from BZH and imidazole-based aldehydes, which showed significant antibacterial activity. Similarly, Słomiak et al. [18] emphasized the antimicrobial potential of chromone-based BZH derivatives to function as antimicrobial agents, while Konstantinović et al. [19] identified isatin-BZH compounds as effective inhibitors of microorganisms. These findings underscore the importance of the BZH core, which is integral to the antibacterial activity of these compounds due to its role in inhibiting bacterial enzymes. However, most studies have focused solely on ligand design without exploring the potential enhancement of antibacterial properties through metal complexation. While Prasanna and Narender [17] noted the hydroxyl group as a synergistic pharmacophore, the effect of different transition metals in combination with hydrazone ligands remains underexplored. Moreover, previous studies have rarely incorporated ADME analysis, which is critical for evaluating drug-like properties of new compounds.

Unlike previous studies [20-22] that focused predominantly on ligand design or individual hydrazone-metal complexes, this research systematically investigates the antibacterial potential of Co(II), Ni(II), Cu(II), and Zn(II) complexes derived from BZH ligands. The study enhances metal coordination by incorporating salicylaldehyde as a hydroxyl-containing pharmacophore, potentially boosting antibacterial activity. Additionally, the inclusion of ADME profiling and molecular docking analyses—rarely explored in similar studies—provides critical insights into these compounds' pharmacokinetic and mechanistic properties. This integrative approach not only fills significant gaps in the literature but also lays a foundation for the development of hydrazone-metal complexes as promising antibacterial agents.

■ EXPERIMENTAL SECTION

Materials

The materials used in this study included 2-hydroxybenzaldehyde (Sigma Aldrich), benzohydrazide (Sigma Aldrich), cobalt(II) chloride hexahydrate (Merck), nickel(II) chloride hexahydrate (Merck), copper(II) chloride dihydrate (Merck), zinc chloride (Merck), ethanol (99.9%, Fulltime), glacial acetic acid (Arkitos), ethyl acetate (Fulltime), chloroform (Merck), sodium acetate (0.5 M, Merck), *S. aureus* ATCC 29213, and *E. coli* ATCC 25922.

Instrumentation

Characterization of the synthesized compounds was conducted using thin-layer chromatography (TLC) plates (silica gel 60 F254, Merck), a UV-vis spectrophotometer (Genesys 10S), an FTIR spectrophotometer (Shimadzu 8400S), an ESI-MS (Q-TOF XEVO), a ^{1}H- and ^{13}C-NMR spectrometer (JEOL RESONANCE 400 MHz), an Analyzer Thermo Scientific Flash Smart Elemental Analyzer, an X-Ray Diffraction (XRD) (PanAnalytical E'xpert Pro), and a TG/DTA analyzer (Hitachi STA7300).

Procedure

Synthesis of ligand

The (*E*)-*N*'-(2-hydroxybenzylidene)benzohydrazide ligand (L) was prepared using our previously established procedures [12]. The spectral data are provided in Fig. S1, and the fragmentation is detailed in Fig. S2.

Synthesis of metal complexes

Initially, 1.5 mmol of L was dissolved in 40 mL of ethanol in a two-neck flask. Subsequently, 1.5 mmol of the M(II) metal (M = Co, Ni, Cu, and Zn) in 10 mL of ethanol was added to the ligand solution. The mixture was refluxed for 2 h, and 1 M CH_3COONa was added dropwise until the pH reached 7–9. The resulting precipitate was filtered, washed several times with ethanol, and dried in a desiccator until a constant mass was achieved.

Antibacterial test

Bacterial cultures of *S. aureus* and *E. coli* were regenerated on nutrient agar (NA) plates. The equipment was sterilized in an autoclave and treated with 70% ethanol before use. A loop of the test bacteria was streaked onto fresh agar plates in a zig-zag pattern. The Petri dishes were sealed with parafilm and incubated upside down at 30 °C for 24 h before refrigeration. Each test sample was dissolved in 1 mL of DMSO at a concentration of 1 mg/mL. Pre-cultures

were prepared by inoculating 1 loopful of bacteria into 20 mL of nutrient broth (NB). NA media was poured into 10 Petri dishes according to the bacterial strain. The pre-cultures were incubated on a shaker at 120 rpm. Absorbance was recorded every 30 min at $\lambda = 630$ nm. Once the absorbance reached 10^9 CFU/mL, 50 µL of the bacterial suspension was spread onto the solid medium using a spreader. The Petri dishes were divided into two quadrants, and filter paper discs (approximately 6 mm in diameter) were placed in each quadrant using forceps. Five microliters of the test solution were applied to each disk. The Petri dishes were incubated at 30 °C for 24 h, and inhibition zones around the filter paper were measured and documented for comparison.

ADME

The Swiss ADME analysis is used to computationally assess the pharmacological characteristics of the test molecules [23]. Both the ligand and the complexes were evaluated virtually using the Swiss ADME tool available at https://www.swissadme.ch. This assessment covers a range of factors, including physicochemical properties, lipophilicity, pharmacokinetic profiles, solubility, and drug-likeness.

Ligand and receptor preparation

ChemDraw was utilized to prepare the ligand and complexes. The samples were then energy-minimized using Avogadro to ensure a convergent structure. The files were converted to *pdbqt format with Open Babel. Then, the target proteins employed in this study included DNA gyrase from *S. aureus* (PDB: 3U2D), which is involved in maintaining DNA topology during replication, and dihydroorotase from *E. coli* (PDB: 2EG7), which catalyzes the reversible cyclization of *N*-carbamoyl-L-aspartate to L-dihydroorotate in pyrimidine nucleotide biosynthesis. Protein preparation involved removing water molecules and native ligands. Any missing atoms in the protein structures were addressed using AutoDockTools, followed by the addition of Kollman charges and polar hydrogens.

Molecular docking

The docking method was validated (RMSD ≤ 2 Å) by re-docking the native ligand to the target protein using AutoDock Tools. The grid center coordinates used were 18.05, −19.454, 5.794 for DNA gyrase from *S. aureus* and 26.326, 40.562, 72.799 for dihydroorotase from *E. coli*, with grid box sizes of $28 \times 16 \times 16$ and $40 \times 40 \times 40$, respectively. To ensure the accuracy of the docking results, 100 Genetic Algorithm (GA) runs and 2,500,000 GA evaluations were employed.

■ RESULTS AND DISCUSSION

Synthesis and Characterization

Compounds synthesis

The hydrazone ligand and Co(II), Ni(II), Cu(II), and Zn(II) complexes (Fig. 1) were successfully synthesized with yields of 21–63%, as shown in Table 1. Elemental analysis revealed that their composition closely matches the theoretical values. All of the complexes are poorly soluble in organic solvents but are soluble in DMSO and DMF.

FTIR analysis

FTIR analysis was conducted to identify the functional groups present in the sample's bonds. The FTIR spectra of the reactant and ligand are displayed in Fig. S3.

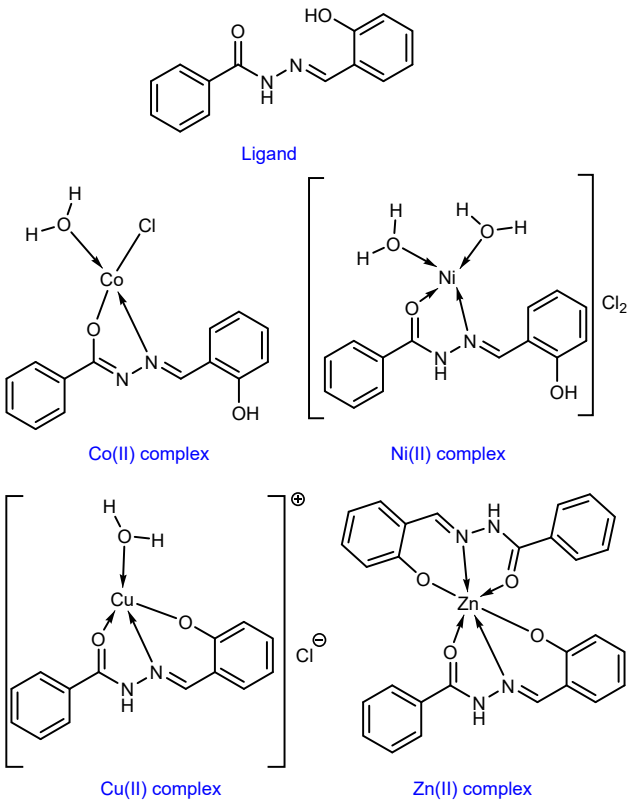

Fig 1. Structure of hydrazone ligand and Co(II), Ni(II), Cu(II), and Zn(II) complexes

Table 1. Physicochemical properties of ligand and metal complexes

Sample	Color	Yield (%)	Elemental analysis experimental (theory)			
			%C	%H	%N	%S
OH ligand	White	62.84	69.96 (69.99)	5.02 (5.03)	11.68 (11.66)	13.34 (13.32)
Co(II) complex	Brown	35.07	47.77 (47.82)	3.66 (3.73)	7.94 (7.97)	13.68 (13.65)
Ni(II) complex	Greenish yellow	20.74	ND	ND	ND	ND
Cu(II) complex	Green	43.58	47.23 (47.20)	3.65 (3.68)	7.84 (7.86)	13.51 (13.47)
Zn(II) complex	Yellow	60.68	61.87 (61.83)	4.05 (4.08)	10.23 (10.30)	11.79 (11.77)

ND: not determined

In contrast, the spectra of the metal complexes are presented in Fig. S4. The FTIR data is summarized in Table 2. The ligand lacks two bands in the wavenumber region around 3200 cm^{-1}, indicating that the primary amine group in BZH has been converted to a hydrazone (–NH–N=CH–) [24]. The position and intensity of the –OH group have merged with the absorption band of the secondary amine, which is linked to intramolecular hydrogen bonding between the –OH and amide groups [25]. The peaks corresponding to aromatic C(sp^2)H and imine are observed at 3058 and 1538 cm^{-1}, respectively [26-27]. The ligand exhibits keto tautomerism, as indicated by the carbonyl peak at 1672 cm^{-1} [25].

The FTIR spectra of the complexes reveal shifts in peak positions. Absorption bands within the wavenumber ranges of 455–475 and 528–588 cm^{-1} suggest the coordination of M–N and M–O bonds [28-30]. The four metal complexes exhibited distinct stereoisomeric profiles. In the Co(II) complex, the amide group undergoes deprotonation to form a tertiary amine around 3200 cm^{-1}, indicating enol tautomerization [31]. This finding is corroborated by the loss of the carbonyl stretching band and the intensified imine absorption resulting from –C=N–N=C–O– resonance [32-34]. Conversely, the C=O vibration observed near 1600 cm^{-1} indicates keto tautomerization in the Ni(II), Cu(II), and Zn(II) complexes.

UV-vis analysis

The UV-vis analysis was conducted to determine the electronic transitions in ligand and complexes. Samples were dissolved in DMSO, and the spectral data, including electronic transitions and their corresponding wavenumbers, are shown in Fig. 2 and summarized in Table 3. The presence of $\pi \rightarrow \pi^*$ and $n \rightarrow \pi^*$ transitions in the ligands is consistent with the aromatic rings, carbonyl, and imine groups. Notably, the observed $n \rightarrow \pi^*$ transition at 287 and 298 nm is higher than that reported for BZH at 267 nm. This bathochromic shift indicates the extension of the conjugated system. A key finding from the spectra of the complexes is the appearance of a new peak at approximately 400 nm, which is attributed to the ligand-to-metal charge transfer (LMCT) transition. This new peak provides strong evidence for the successful formation of the metal complexes.

Thermogravimetric analysis

Thermogravimetric analysis of the complexes was performed in a nitrogen atmosphere at a heating rate of 10 °C/min. Thermograms are provided in Fig. S5 and summarized in Table 4. The cobalt(II) complex exhibits

Table 2. FTIR of ligand and Co(II), Ni(II), Cu(II), and Zn(II) complexes

Sample	Wavenumber (cm^{-1})							
	–OH	$–NH_2$	–NH	–C(sp^2)H	–C=O	–C=N	M–O	M–N
BZH	-	3195	3298	3049	1659	-	-	-
Ligand	3268	-	3268	3058	1672	1538	-	-
Co(II) complex	3384	-	-	3045	-	1536	528	470
Ni(II) complex	3355	-	-	3047	1600	1556	527	475
Cu(II) complex	3375	-	3271	3021	1624	1555	532	455
Zn(II) complex	-	-	3271	3002	1612	1571	588	464

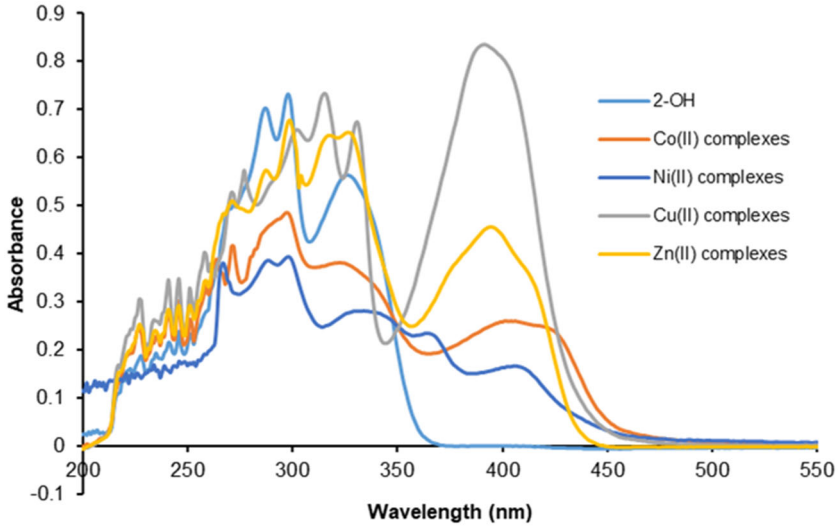

Fig 2. UV-vis spectra of ligand and complex compounds

Table 3. UV-vis analysis of ligand and Co(II), Ni(II), Cu(II), and Zn(II) complexes

Transition	Wavenumber (nm)				
	Ligand	Co(II) complex	Ni(II) complex	Cu(II) complex	Zn(II) complex
$\pi \rightarrow \pi^*$	207, 219, 223, 228, 235, 241, 246, 251	227, 238, 241, 246, 251, 259, 264	221, 226, 234, 239, 246, 253, 267, 289	227, 234, 241, 246, 251, 258, 271, 277	227, 235, 241, 246, 259, 271, 288
$n \rightarrow \pi^*$	287, 298, 326	297, 323	298, 334, 364	305, 315, 331	298, 304, 318, 327
LMCT	-	406	407	392	395

Table 4. Thermogravimetric analysis of Co(II), Ni(II), Cu(II), and Zn(II) complexes

Compound	Stage	Temperature range (°C)	%Mass loss (experimental)	%Mass loss (theoretical)	Moieties
Co(II) complex	1	278–354	36.33	34.16	C_7H_6NO
	2	354–503	34.24	33.87	C_7H_5NO
	3	503–569	10.16	10.07	H_2Cl
		Residue	19.27	21.31	CoO
Ni(II) complex	1	48–105	20.66	20.43	CCl_2
	2	337–440	41.71	41.43	$C_7H_8N_2O_3$
	3	440–600	4.83	4.44	H_2O
		Residue	33.63	33.71	NiC_6H_6
Cu(II) complex	1	29–87	9.08	9.95	Cl
	2	310–840	64.64	64.35	$C_{13}H_{12}N_2O_2$
		Residue	26.32	25.70	CuO + C
Zn(II) complex	1	352–379	39.74	38.65	$C_{13}H_{10}N_2O$
	2	462–900	43.63	44.17	$C_{14}H_{12}N_2O_2$
		Residue	16.69	17.17	ZnO + C

three distinct stages of mass loss. The initial stage, occurring between 278–354 °C, resulted in a 36.33% mass reduction attributed to the decomposition of the C_7H_6NO ligand. The subsequent mass loss of the C_7H_5NO species was observed between 354–503 °C. The final stage, with a mass loss of 10.16% at 503–569 °C, indicated the elimination of H_2Cl, leaving cobalt oxide (CoO) as a residue [35].

A similar decomposition pattern was observed for the nickel(II) complex. The first stage, with a 20.66% mass

loss between 48–105 °C, was associated with the removal of CCl_2. The second stage, occurring between 337–440 °C, showed a 41.71% mass loss, identified as $C_7H_8N_2O_3$. The final stage, 440–600 °C, involved a mass loss of 4.82%, corresponding to coordinated water. The residual char content (33.63%) indicated nickel carbon (NiC_6H_6) [34].

The copper(II) and zinc(II) complexes underwent two decomposition stages. For the copper(II) complex, a 9.08% mass loss between 29–87 °C was attributed to the loss of the Cl counterion, whereas a 64.64% mass loss between 310–840 °C corresponded to the decomposition of the $C_{13}H_{12}N_2O_2$. In the zinc(II) complex, mass losses of 39.74% between 352–379 °C and 43.63% between 462–900 °C were associated with the decomposition of the $C_{13}H_{10}N_2O$ and $C_{14}H_{12}N_2O_2$, respectively. The final decomposition products of both samples were metal oxides and carbon [36].

XRD analysis

XRD characterization is conducted to determine the structure and crystal size of M(II)-hydrazone complexes (M = Co, Ni, Cu, and Zn). The sample's diffractogram is provided in Fig. S6. Based on the Debye-Scherrer equation [37], the average crystal sizes for the Co(II), Ni(II), Cu(II), and Zn(II) complexes are 34.41, 18.27, 17.59, and 44.70 nm, respectively. The nanoparticle size enhances the sample's ability to permeate cell membranes [38]. The powder XRD diffractogram was refined using the Rietveld Le-Bail method within the Rietica software [39]. The Rietveld method involves a nonlinear fitting technique between the sample's diffraction pattern and a standard, employing a least squares approach [40-41]. The refinement of the Co(II), Ni(II), and Cu(II) complexes was compared with data from the IUCr electronic archives (SU2089) or CCDC 606531 [42], while the Zn(II) complex was compared with data from Al-Qadsy et al. [34].

The results of the refinement are illustrated in Fig. S7. The red, black, and green peaks correspond to the reference data, sample data, and the difference between the reference and sample, respectively. The refinement provided Rp, Rwp, and χ^2 values listed in Table 5. These values adhere to the standards (Rwp < 20 and $\chi^2 < 4$), indicating a satisfactory fit between the sample and reference materials [43]. All complex compounds exhibit a triclinic crystal system.

ADME Study

The physicochemical profiles of the ligand and complexes are detailed in Table 6. Molecular weight is a crucial parameter for the transvascular transport of therapeutic agents [44]. The number of hydrogen bond donors and acceptors impacts the acid-base characteristics of the molecule [45]. Lipophilicity affects the drug's ability to cross membranes, enhancing its distribution throughout the body via the bloodstream.

According to the ADME investigation results, both the ligand and the complex compounds conform to

Table 5. XRD analysis of complexes

	Co(II) complex	Ni(II) complex	Cu(II) complex	Zn(II) complex
Particle size (Debby Scherrer) (nm)	34.414	18.271	17.593	44.697
	Refinement with the Rietica application			
Standard	Tamboura et al. [42]			Al-Qadsy et al. [34]
Rp	9.14	14.18	15.577	18.59
Rwp	11.22	15.55	17.887	15.94
χ^2	0.032	0.017	0.016	0.577
Crystal system	Triclinic	Triclinic	Triclinic	Triclinic
a	6.762876	6.789713	6.644	11.778
b	9.017858	9.235840	9.425	6.463
c	10.420684	10.496758	10.523	17.939
α	77.548004	77.248573	75.431	87.804
β	84.675	86.597	84.457	106.327
γ	81.671	81.518	82.016	89.976

Lipinski's rules, although the molecular weight of the Zn(II) complex slightly exceeds 500 g/mol. Lipinski's rules are essential for evaluating the suitability of compounds as orally active drugs in humans [46]. Commonly known as the "rule of five," these guidelines specify parameters such as a molecular weight < 500, hydrogen bond donors < 5, hydrogen bond acceptors < 10, and an octanol-water partition coefficient < 5 [47]. The topological polar surface area (TPSA) measures the contribution of functional groups to the polar surface area of the molecule [48]. All samples fall within the standard TPSA range (20–130 Å), indicating that the target compounds have bioavailability when administered *in vivo* in rodents [49].

The samples' pharmacokinetic profiles and water solubility are summarized in Table 7. The Zn(II) complex shows notably low solubility in water compared to the other samples, attributed to its larger size and a metal-to-ligand ratio of 1:2. While all compounds exhibit a high likelihood of gastrointestinal absorption, they have limited potential for skin penetration, as evidenced by log Kp values below −2 cm/s [50]. This suggests that the target compounds are more suited for oral administration rather than transdermal delivery. The blood-brain barrier (BBB) parameter assesses the ability of central nervous system blood vessels to regulate the movement of ions and molecules between the blood and the brain [51]. The drug-likeness profiles of the ligand and complexes are detailed in Table 8. All five samples exhibit bioavailability scores (BS), with the Cu(II) complex reaching a score of 0.85. This suggests that all test

Table 6. Physicochemical and lipophilicity profiles of ligands and complexes

	Ligand	Co(II) complex	Ni(II) complex	Cu(II) complex	Zn(II) complex
Formula	$C_{14}H_{12}N_2O_2$	$C_{14}H_{13}ClCoN_2O_3$	$C_{14}H_{16}Cl_2NiN_2O_4$	$C_{14}H_{13}ClCuN_2O_3$	$C_{28}H_{22}ZnN_4O_4$
Mr (g/mol)	240.26	351.65	405.89	356.26	543.88
H-bond donor	2	2	4	2	2
H-bond acceptor	3	4	4	3	4
Molar refractivity	69.93	85.68	94.68	84.38	150.96
TPSA (Å)	61.69	63.41	80.15	59.92	101.38
log $P_{o/w}$ (iLOGP)	1.95	0.00	0.00	0.00	0.00
log $P_{o/w}$ (XLOGP3)	3.01	3.24	3.52	3.50	6.34
log $P_{o/w}$ (WLOGP)	2.16	2.52	2.64	−1.53	3.06
log $P_{o/w}$ (MLOGP)	2.28	1.72	1.16	1.72	3.78
log $P_{o/w}$ (SILICOS-IT)	2.46	0.23	−3.36	−2.12	−1.84
Consensus log $P_{o/w}$	2.37	1.54	0.79	0.31	2.27

Table 7. Pharmacokinetic profile and water solubility of ligands and complex compounds

	Ligand	Co(II) complex	Ni(II) complex	Cu(II) complex	Zn(II) complex
log S (ESOL)	−3.46	−4.35	−4.83	−4.61	−7.55
Solubility (mg/mL)	8.42×10^{-2}	1.56×10^{-2}	6.03×10^{-3}	8.73×10^{-3}	1.52×10^{-5}
Class	Soluble	Moderately soluble	Moderately soluble	Moderately soluble	Poorly soluble
log S (Ali)	−3.97	−4.24	−4.89	−4.44	−8.26
Solubility (mg/mL)	2.57×10^{-2}	2.00×10^{-2}	5.26×10^{-3}	1.29×10^{-2}	2.99×10^{-6}
Class	Soluble	Moderately soluble	Moderately soluble	Moderately soluble	Poorly soluble
log S (SILICOS-IT)	−4.44	−5.33	−5.10	−5.37	−10.35
Solubility (mg/mL)	8.72×10^{-3}	1.66×10^{-3}	3.25×10^{-3}	1.51×10^{-3}	2.45×10^{-8}
Class	Moderate soluble	Moderate soluble	Moderate soluble	Moderately soluble	Insoluble
GI Absorption	High	High	High	High	High
BBB-Permeant	Yes	Yes	No	No	No
log Kp (skin permeation) (cm/s)	−5.63	−6.14	−6.28	−5.99	−5.12

Table 8. Drug-likeness profile in water ligands and complex compounds

	OH	Co(II) complex	Ni(II) complex	Cu(II) complex	Zn(II) complex
Lipinski	Yes	Yes	Yes	Yes	Yes (1 violation)
Ghose	Yes	Yes	Yes	No (1 violation)	No (2 violation)
Veber	Yes	Yes	Yes	Yes	Yes
Egan	Yes	Yes	Yes	Yes	Yes
Muegge	Yes	Yes	Yes	Yes	No (2 violation)
Bioavailability score	0.55	0.55	0.55	0.85	0.85
Synthetic accessibility	2.29	4.34	3.52	4.28	4.84

Table 9. Antibacterial test of ligand and metal complexes

Sample	Average zone of inhibition (mm)	
	S. aureus	*E. coli*
Ligand	7.8 ± 1.8	7.5 ± 0.30
Co(II) complex	-	8.95 ± 1.15
Ni(II) complex	12.3 ± 2.1	12.55 ± 1.15
Cu(II) complex	19.7 ± 4.2	13.45 ± 0.05
Zn(II) complex	12.4 ± 1.3	8.6 ± 0.50

compounds have a bioavailability (F) exceeding 10% in rodent models, making them appropriate for oral administration [52].

In Vitro Study

The antibacterial activity was assessed using the disk diffusion method against Gram-positive (*S. aureus*) and Gram-negative bacteria (*E. coli*). Table 9 presents the inhibition zone data for the ligand and its metal complexes, detailed in Table S1. The ligand exhibited average inhibition zones of 7.8 ± 1.8 and 7.5 ± 0.3 mm against *S. aureus* and *E. coli*, respectively. Upon forming metal complexes, the inhibition zones generally increased, with the exception of the Co(II) complex against *S. aureus*, which showed no inhibition. These findings suggest that the metal complexes have potential as antibacterial agents. The Cu(II) complex demonstrated the most effective inhibition, with zones measuring 19.7 ± 4.2 and 13.45 ± 0.05 mm against *S. aureus* and *E. coli*, respectively.

In Silico Study

The molecular docking analysis of ligand-protein interactions was performed using AutodockTools 4.2. The ligands were docked to the topoisomerase protein "DNA gyrase" in *S. aureus* and the hydrolase protein "dihydroorotase" in *E. coli*. These proteins are involved in maintaining DNA topology stability during replication and in the pyrimidine nucleotide biosynthesis pathway [53-54]. Method validation was carried out by re-docking the native ligands to their corresponding proteins, ensuring accuracy by removing water molecules, adding polar hydrogens, and applying Gasteiger charges. The best docking poses were selected based on an RMSD ≤ 2 Å, with values of 1.85 (08B) and 1.81 Å (OTD). Fig. 3 displays the optimal poses of the native ligands, using PyMOL integrated with PLIP Tools.

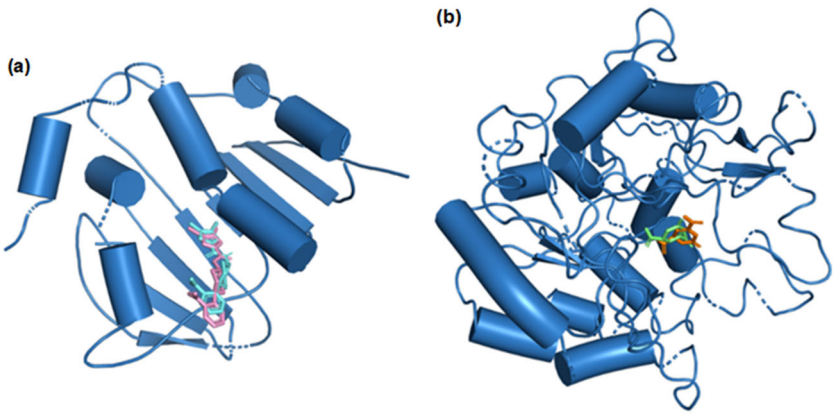

Fig 3. The superimposed results of (a) re-docking (aquamarine) with the native ligand (pink) on DNA gyrase *S. aureus* and (b) re-docking (lime) with the native ligand (orange) on dihydroorotase *E. coli*

The docking protocol was applied to all compound samples in accordance with the validated method. The binding energy obtained from this study measures the compound's affinity for the target protein, with lower binding energy values indicating stronger interactions. Additionally, the Ki (inhibition constant) values were calculated, reflecting the compounds' potential to inhibit the target protein. These findings are summarized in Fig. 4 and Tables 10 and 11. The hydrogen bond interactions between the sample compounds and the native ligand (08B) were found to involve the identical residues—Arg81, Arg84, and Thr173—within the active site of *S. aureus* DNA gyrase (Fig. 5). Similarly, interactions between the sample compounds and the native ligand (OTD) occurred at common residues, including His18, Arg20, Asn44, and Asp250 (Fig. 6).

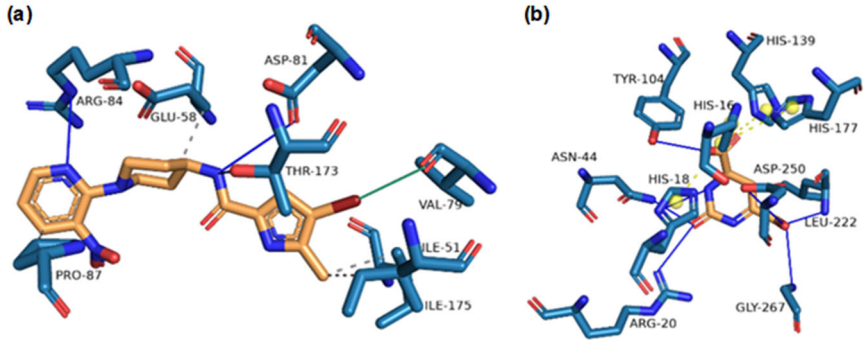

Fig 4. Visualization of hydrogen bond interactions (in blue) occurring at (a) DNA gyrase residues with the native ligand (08B) and (b) dihydroorotase residues with the native ligand (OTD)

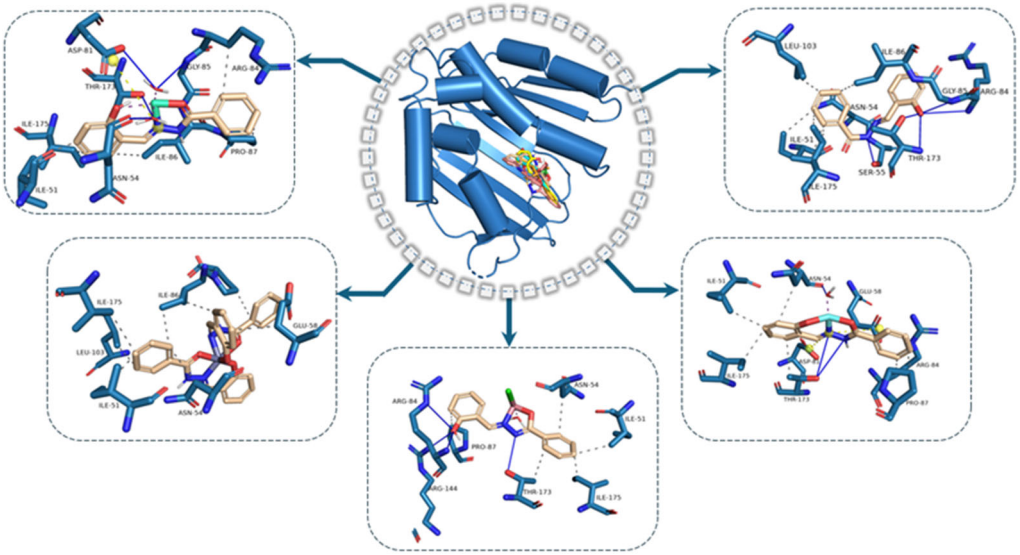

Fig 5. The docked compounds with DNA gyrase *S. aureus* (from top right to top left: ligand, Cu, Co, Zn, Ni)

Table 10. Molecular docking results against DNA gyrase

Compound	Binding energy (kcal/mol)	Ki (μM)	Residue interaction
Ligand	−9.22	0.17	Ser55, **Arg84**, Gly85, **Thr173**
Co(II) complex	−9.15	0.19	**Arg84**, Arg144, **Thr173**
Ni(II) complex	−8.50	0.58	-
Cu(II) complex	−8.20	0.97	Asn54, **Thr173**
Zn(II) complex	−8.36	0.74	Asn54, **Asp81**, Gly85, **Thr173**
Native ligand (08B)	−7.05	6.81	**Arg81**, **Arg84**, **Thr173**

Table 11. Molecular docking results against dihydroorotase

Compound	Binding energy (kcal/mol)	Ki (μM)	Residue interaction
Ligand	−6.84	9.67	**Arg20**, **Asn44**, His254
Co(II) complex	−7.87	1.72	**Arg20**, **Asn44**, **Asp250**
Ni(II) complex	−9.76	0.07	**Asn44**
Cu(II) complex	−7.45	3.47	**His18**, **Arg20**, **Asn44**, Ala266
Zn(II) complex	−7.19	5.33	**Asn44**
Native ligand (OTD)	−7.97	1.44	**His18**, **Arg20**, **Asn44**, Tyr104, Leu222, **Asp250**, Gly267

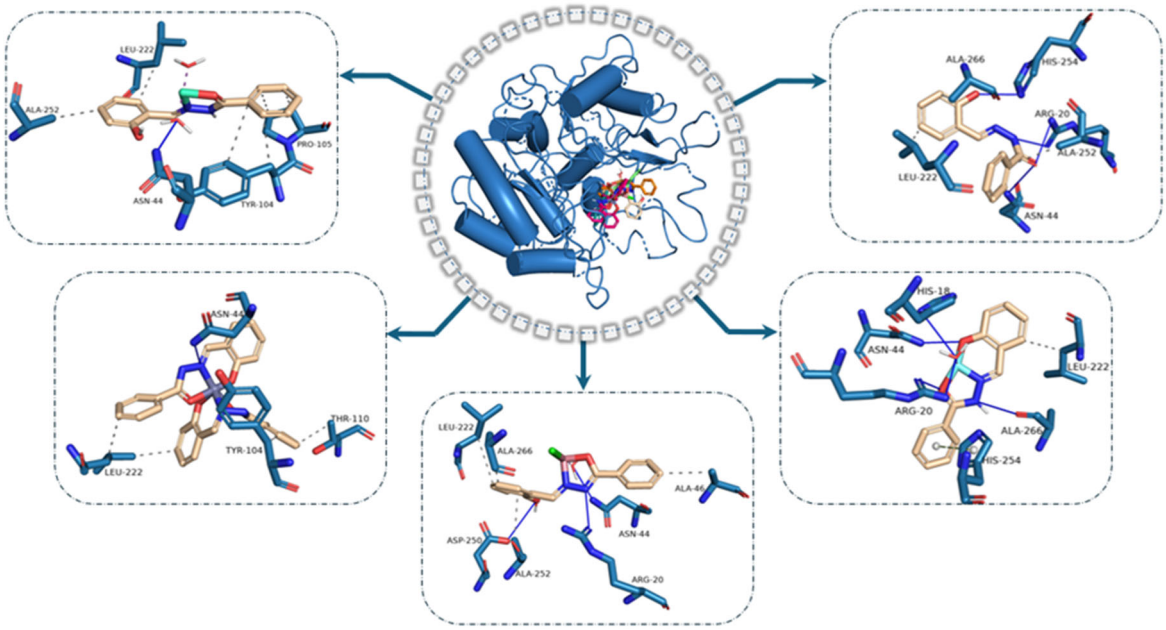

Fig 6. The docked compounds with dihydroorotase *E. coli* (from top right to top left: ligand, Cu, Co, Zn, Ni)

■ CONCLUSION

We successfully synthesized four hydrazone-based complexes with Co(II), Ni(II), Cu(II), and Zn(II) derived from benzohydrazide and salicylaldehyde. The ligand exhibited bidentate coordination in the Co(II) and Ni(II) complexes and tridentate coordination in the Cu(II) and Zn(II) complexes. ADME study confirmed that the ligand and complexes adhere to Lipinski's rule of five. *In vitro* assays indicated that the complexes exhibited stronger activity than the ligand against *S. aureus* and *E. coli*, with the Cu(II) complex demonstrating the highest efficacy. Molecular docking studies revealed interactions at the same active site residues as those observed for the native ligands.

■ ACKNOWLEDGMENTS

The authors express their gratitude to the National Research and Innovation Agency (BRIN) for supporting their work through the “Research and Innovation for Indonesia’s Progress” (RIIM) program, under grant number B-3450//II.7.5/FR.06.00/7/2023 and the Ministry of Education, Culture, Research, and Technology (KEMDIKBUDRISTEK) RI through the program "Doctoral Dissertation Research" (PDD), grant number 017/C3/DT.05.00/PL/2025.

■ CONFLICT OF INTEREST

The authors declare no conflict of interest.

■ AUTHOR CONTRIBUTIONS

Mardi Santoso and Fahimah Martak were involved in supervising and conceiving the study's experimental design in the provision of resources and funding. Yusuf Syahril Alam, Nuraini Fitria, Amelia Bella Putri Adama, Shava Alivifia Salsabilla, and Shinta Ratna Duhita conducted a synthesis experiment and bioactivity test,

data collection, and analysis. Yusuf Syahril Alam performed docking analysis. Yusuf Syahril Alam, Mardi Santoso, and Fahimah Martak wrote and revised the manuscript. All authors agreed to the final version of this manuscript.

■ REFERENCES

[1] Varghese, M., and Balachandran, M., 2021, Antibacterial efficiency of carbon dots against gram-positive and gram-negative bacteria: A review, *J. Environ. Chem. Eng.*, 9 (6), 106821.

[2] Dawodu, O.G., and Akanbi, R.B., 2021, Isolation and identification of microorganisms associated with automated teller machines on Federal Polytechnic Ede campus, *PLoS One*, 16 (8), e0254658.

[3] Wang, T.Y., Zhu, X.Y., and Wu, F.G., 2023, Antibacterial gas therapy: Strategies, advances, and prospects, *Bioact. Mater.*, 23, 129–155.

[4] Ding, D., Wang, B., Zhang, X., Zhang, J., Zhang, H., Liu, X., Gao, Z., and Yu, Z., 2023, The spread of antibiotic resistance to humans and potential protection strategies, *Ecotoxicol. Environ. Saf.*, 254, 114734.

[5] Murray, C.J.L., Ikuta, K.S., Sharara, F., Swetschinski, L., Robles Aguilar, G., Gray, A., Han, C., Bisignano, C., Rao, P., Wool, E., Johnson, S.C., Browne, A.J., Chipeta, M.G., Fell, F., Hackett, S., Haines-Woodhouse, G., Kashef Hamadani, B.H., Kumaran, E.A.P., McManigal, B., Achalapong, S., Agarwal, R., Akech, S., Albertson, S., Amuasi, J., Andrews, J., Aravkin, A., Ashley, E., Babin, F.X., Bailey, F., Baker, S., Basnyat, B., Bekker, A., Bender, R., Berkley, J.A., Bethou, A., Bielicki, J., Boonkasidecha, S., Bukosia, J., Carvalheiro, C., Castañeda-Orjuela, C., Chansamouth, V., Chaurasia, S., Chiurchiù, S., Chowdhury, F., Clotaire Donatien, R., Cook, A.J., Cooper, B., Cressey, T.R., Criollo-Mora, E., Cunningham, M., Darboe, S., Day, N.P.J., De Luca, M., Dokova, K., Dramowski, A., Dunachie, S.J., Duong Bich, T., Eckmanns, T., Eibach, D., Emami, A., Feasey, N., Fisher-Pearson, N., Forrest, K., Garcia, C., Garrett, D., Gastmeier, P., Giref, A.Z., Greer, R.C., Gupta, V., Haller, S., Haselbeck, A., Hay, S.I., Holm, M., Hopkins, S., Hsia, Y., Iregbu, K.C., Jacobs, J., Jarovsky, D., Javanmardi, F., Jenney, A.W.J., Khorana, M., Kissoon, N., Kobeissi, E., Kostyanev, T., Phommasone, K., Khusuwan, S., Krapp, F., Krumkamp, R., Kumar, A., Kyu, H.H., Lim, C., Lim, K., Limmathurotsakul, D., Loftus, M.J., Lunn, M., Ma, J., Manoharan, A., Marks, F., May, J., Mayxay, M., Mturi, N., Munera-Huertas, T., Musicha, P., Musila, L.A., Mussi-Pinhata, M.M., Naidu, R.N., Nakamura, T., Nanavati, R., Nangia, S., Newton, P., Ngoun, C., Novotney, A., Nwakanma, D., Obiero, C.W., Ochoa, T.J., Olivas-Martinez, A., Olliaro, P., Ooko, E., Ortiz-Brizuela, E., Ounchanum, P., Pak, G.D., Paredes, J.L., Peleg, A.Y., Perrone, C., Phe, T., Plakkal, N., Ponce-de-Leon, A., Raad, M., Ramdin, T., Rattanavong, S., Riddel, A., Roberts, T., Robotham, J.V., Roca, A., Rosenthal, V.D., Rudd, K.E., Russell, N., Sader, H.S., Saengchan, W., Schnall, J., Scott, J.A.G., Seekaew, S., Sharland, M., Shivamallappa, M., Sifuentes-Osornio, J., Simpson, A.J., Steenkeste, N., Stewardson, A.J., Stoeva, T., Tasak, N., Thaiprakong, A., Thwaites, G., Tigoi, C., Turner, C., Turner, P., van Doorn, H.R., Velaphi, S., Vongpradith, A., Vongsouvath, M., Vu, H., Walsh, T., Walson, J.L., Waner, S., Wangrangsimakul, T., Wannapinij, P., Wozniak, T., Young-Sharma, T.E.M.W., Yu, K.C., Zheng, P., Sartorius, B., Lopez, A.D., Stergachis, A., Moore, C., Dolecek, C., and Naghavi, M., 2022, Global burden of bacterial antimicrobial resistance in 2019: A systematic analysis, *Lancet*, 399 (10325), 629–655.

[6] Kölmel, D.K., and Kool, E.T., 2017, Oximes and hydrazones in bioconjugation: Mechanism and catalysis, *Chem. Rev.*, 117 (15), 10358–10376.

[7] Santoso, M., Fahmi, M.R.G., Kurniawan, Y.S., Ersam, T., Fatmawati, S., Martak, F., and Fadlan, A., 2021, Isoniazid-isatin hydrazone derivatives: Synthesis, antitubercular activity and molecular docking studies, *Trends Sci.*, 18 (21), 39.

[8] Firmino, G.S.S., de Souza, M.V.N., Pessoa, C., Lourenco, M.C.S., Resende, J.A.L.C., and Lessa, J.A., 2016, Synthesis and evaluation of copper(II) complexes with isoniazid-derived hydrazones as anticancer and antitubercular agents, *Biometals*, 29 (6), 953–963.

[9] Alotabi, S.H., 2020, Synthesis, characterization, anticancer activity, and molecular docking of some

new sugar hydrazone and arylidene derivatives, *Arabian J. Chem.*, 13 (3), 4771–4784.

[10] El-saied, F.A., Shakdofa, M.M.E., Al-Hakimi, A.N., and Shakdofa, A.M.E., 2020, Transition metal complexes derived from *N′*-(4-fluorobenzylidene)-2-(quinolin-2-yloxy) acetohydrazide: Synthesis, structural characterization, and biocidal evaluation, *Appl. Organomet. Chem.*, 34 (11), e5898.

[11] Pallapati, R.K., Mutchu, B.R., Khandapu, B.M.K., Vanga, U.R., Varala, R., and Bollikolla, H.B., 2020, Synthesis of novel gabapentin scaffold derived hydrazide-hydrazones for potential antimicrobial agents and antioxidants, *Chem. Afr.*, 3 (4), 881–888.

[12] Alam, Y.S., Pudjiastuti, P., Maulana, S., Affifah, N.R., Martak, F., Fadlan, A., Wahyuni, T.S., and Arief, S., 2023, Synthesis and antidiabetic evaluation of *N*'-benzylidenebenzohydrazide derivatives by *in silico* studies, *Indones. J. Chem.*, 23 (4), 1061–1070.

[13] Abidiy, S.I., Gunawan, T., Alam, Y.S., Fadlan, A., Purnomo, A.S., Martak, F., Pudjiastuti, P., and Arief, S., 2024, Antiviral activity of hydrazone derivatives based benzohydrazide/2-thiohydantoin analogs against HPV-18 (human papillomavirus): *In silico* study, *AIP Conf. Proc.*, 3071 (1), 020015.

[14] Al Furaiji, K.H.M., Al Hassani, R.A.M., and Hussein, H.H., 2024, Synthesis and antibacterial activity of azomethine ligand and their metal complexes: A combined experimental and theoretical study, *Indones. J. Chem.*, 24 (1), 54–66.

[15] Sevda, E.R., Ünver, H., and Dikmen, G., 2023, A new dinuclear copper(II)-hydrazone complex: Synthesis, crystal, structure and antibacterial activity, *Lett. Org. Chem.*, 20 (4), 376–387.

[16] Avaji, P.G., Vinod Kumar, C.H., Patil, S.A., Shivananda, K.N., and Nagaraju, C., 2009, Synthesis, spectral characterization, *in-vitro* microbiological evaluation and cytotoxic activities of novel macrocyclic bis hydrazone, *Eur. J. Med. Chem.*, 44 (9), 3552–3559.

[17] Laxmi Prasanna, V., and Narender, R., 2015, Synthesis and antimicrobial activity of new imidazole-hydrazone derivatives, *Asian J. Chem.*, 27 (10), 3605–3608.

[18] Słomiak, K., Łazarenkow, A., Chęcińska, L., Kusz, J., Ochocki, J., and Nawrot-Modranka, J., 2018, Synthesis, spectroscopic analysis and assessment of the biological activity of new hydrazine and hydrazine derivatives of 3-formylchromone, *Molecules*, 23 (8), 2067.

[19] Konstantinović, S.S., Tomić, J., Savić, J., Zlatković, M., Mirković, J.J., and Dugalić, G.V.S., 2015, The synthesis and antimicrobial activity of isatin-3-(4'-hydroxy) benzoylhydrazone, *Adv. Technol.*, 4 (1), 49–53.

[20] Adam, M.S.S., Shaaban, S., Khalifa, M.E., Alhasani, M., and El-Metwaly, N., 2021, New Cu(II) and VO(II)-O,N,O-aroylhydrazone complexes: Biological evaluation, catalytic performance, *ct*DNA interaction, DFT, pharmacophore, and docking simulation, *J. Mol. Liq.*, 335, 116554.

[21] Ahmad, F., Alkahtani, M.D.F., Taj, M.B., Alnajeebi, A.M., Alzahrani, S.O., Babteen, N.A., Alelwani, W., Bannunah, A.M., Noor, S., Ayub, R., Tirmizi, S.A., and Alshater, H., 2021, Synthesis of new naphthyl aceto hydrazone-based metal complexes: Micellar interactions, DNA binding, antimicrobial, and cancer inhibition studies, *Molecules*, 26 (4), 1044.

[22] Kothari, R., Agrawal, A., and Rai, S., 2022, Molecular docking and antibacterial activities of cobalt(II) complexes derived from precursors of hydrazones, *Indian J. Biochem. Biophys.*, 59 (6), 640–652.

[23] Daina, A., Michielin, O., and Zoete, V., 2017, SwissADME: A free web tool to evaluate pharmacokinetics, drug-likeness and medicinal chemistry friendliness of small molecules, *Sci. Rep.*, 7 (1), 42717.

[24] Moreira, J.M., Vieira, S.S.F., Correia, G.D., de Almeida, L.N., Finoto, S., Brandl, C.A., Msumange, A.A., Galvão, F., Pires de Oliveira, K.M., Caneppele Paveglio, G., da Silva, M.M., Tirloni, B., da Carvalho, C.T., and Roman, D., 2025, Synthesis and characterization of novel hydrazone complexes: exploring DNA/BSA binding and antimicrobial potential, *ACS Omega*, 10 (7), 7428–7440.

[25] Burgos-Lopez, Y., Del Plá, J., Balsa, L.M., León, I.E., Echeverría, G.A., Piro, O.E., García Tojal, L., Pis-Diez, R., González-Baró, A.C., and Parajón-Costa,

B.S., 2019, Synthesis, crystal structure and cytotoxicity assays of a copper(II) nitrate complex with a tridentate ONO acylhydrazone ligand. Spectroscopic and theoretical studies of the complex and its ligand, *Inorg. Chim. Acta*, 487, 31–40.

[26] Manikandan, V., Balaji, S., Senbagam, R., Vijayakumar, R., Rajarajan, M., Vanangamudi, G., Arulkumaran, R., Sundararajan, R., and Thirunarayanan, G., 2017, Synthesis and antimicrobial activities of some (*E*)-*N*'-1-(substituted benzylidene)benzohydrazide, *Int. J. Adv. Chem.*, 5 (1), 17–24.

[27] Setyawati, A., Wahyuningsih, T.D., and Purwono, B., 2017, Synthesis and characterization of novel benzohydrazide as potential antibacterial agents from natural product vanillin and wintergreen oil, *AIP Conf. Proc.*, 1823 (1), 020121.

[28] Al-Hazmi, G.A.A., and El-Metwally, N., 2017, A series of nickel(II) complexes derived from hydrazide derivatives, electrochemical, thermal and spectral studies, *Arabian J. Chem.*, 10 (Suppl. 1), S1003–S1013.

[29] Mandewale, M.C., Kokate, S., Thorat, B., Sawant, S., and Yamgar, R., 2019, Zinc complexes of hydrazone derivatives bearing 3,4-dihydroquinolin-2(1*H*)-one nucleus as new anti-tubercular agents, *Arabian J. Chem.*, 12 (8), 4479–4489.

[30] Zuhair, F.H., Al-Garawi, Z.S., Al-Jibouri, M.N., Mohamed, G.G., and Abdallah, A.M., 2024, Synthesis, physical, chemical and DFT properties of cobalt(II), nickel(II), copper(II), and zinc(II) complexes with polydentate Schiff base derived from 1,2,4-triazole, *Indones. J. Chem.*, 24 (4), 1034–1045.

[31] Basaran, E., Sogukomerogullari, H.G., Tılahun Muhammed, M., and Akkoc, S., 2024, Synthesis of novel Cu(II), Co(II), Fe(II), and Ni(II) hydrazone metal complexes as potent anticancer agents: Spectroscopic, DFT, molecular docking, and MD simulation studies, *ACS Omega*, 9 (38), 40172–40181

[32] Ayyannan, G., Mohanraj, M., Raja, G., Bhuvanesh, N., Nandhakumar, R., and Jayabalakrishnan, C., 2016, New palladium(II) hydrazone complexes, synthesis, structure and biological evaluation, *J. Photochem. Photobiol., B*, 163, 1–13.

[33] Deng, J.G., Gou, Y., Cheng, W., Fu, X., and Deng, H., 2016, The Cu/ligand stoichiometry effect on the coordination behavior of aroyl hydrazone with copper(II): Structure, anticancer activity and anticancer mechanism, *Bioorg. Med. Chem.*, 24 (10), 2190–2198.

[34] Al-Qadsy, I., Al-Odayni, A.B., Saeed, W.S., Al-rabie, A., Al-Adhreai, A., Al-Faqeeh, L.A.S., Lama, P., Alghamdi, A.A., and Farooqui, M., 2021, Synthesis, characterization, single-crystal X-ray structure and biological activities of [*Z*-*N*'-(4-methoxybenzylidene)benzohydrazide-nickel(II)] complex, *Crystal*, 11 (2), 110.

[35] Aldoghachi, R.J.K., Aldoghachi, F.A.J., Alsalim, T.A.Q., and Ibrahim, M.L., 2022, Synthesis, thermal analysis, and thermodynamic properties study of new quinoline derivative and their V(IV), Co(II), and Cu(II) complexes, *Indones. J. Chem.*, 22 (5), 1376–1385.

[36] Aly, S.A., Hassan, S.S., El-Boraey, H.A., Eldourghamy, A., Abdalla, E.M., Alminderej, F.M., and Elganzory, H.H., 2024, Synthesis, biological activity, and the effect of ionization radiation on the spectral, XRD, and TGA analysis of Cu(I), Cu(II), Zn(II), and Cd(II) complexes, *Arabian J. Sci. Eng.*, 49 (1), 361–379.

[37] Khedr, A.K., Zaky, R.R., Gomaa, E.A., and Abd El-Hady, M.N., 2022, Elucidation for coordination features of N-(benzothiazol-2-yl)-3-oxo-3-(2-(3-phenylallylidene)hydrazineyl)propanamide on Co^{2+}, Ni^{2+} and Cu^{2+}: Structural description, DFT geometry optimization, cyclic voltammetry and biological inspection, *J. Mol. Liq.*, 368, 120613.

[38] Kumar, N., Kaushal, R., Chaudhary, A., Arora, S., and Awasthi, P., 2019, Titanium based mixed ligand complexes: Synthesis, spectroscopic and in vitro antiproliferative studies, *Inorg. Nano-Met. Chem.*, 48 (9), 467–476.

[39] Sugiyarto, K.H., Yunita, I., and Goodwin, H.A., 2020, Preparation, electronic properties, and powder-XRD structure analysis of 3,5-bis(pyridin-2-yl)-*H*-1,2,4-triazoledichloridocopper(II), *Indones. J. Chem.*, 20 (6), 1422–1429.

[40] Hidayat, N., Hidayat, A., Hidayat, S., Mufti, N., Taufiq, A., and Heriyanto, H., 2019, Assessing

Rietveld refinement results on silicon carbide nanoparticles produced by magnesiothermal treatment, *J. Phys.: Conf. Ser.*, 1595 (1), 012032.

[41] Evans, J.S.O., and Evans, I.R., 2021, Structure analysis from powder diffraction data: Rietveld refinement in excel, *J. Chem. Educ.*, 98 (2), 495–505.

[42] Tamboura, F.B., Gaye, M., Sall, A.S., Barry, A.H., and Bah, Y., 2009, Chlorido[*N*'-(2-oxidobenzilidene)aceto hydrazide-κ^2*O*,*N*',*O*']copper(II) dehydrate, *Acta Crystallogr., Sect. E: Crystallogr. Commun.*, 65 (2), m160–m161.

[43] Purwaningsih, S.Y., Rosidah, N., Zainuri, M., Triwikantoro, T., Pratapa, S., and Darminto, D., 2019, Comparation of X-ray diffraction pattern refinement using Rietica and MAUD of ZnO nanoparticles and nanorods, *J. Phys.: Conf. Ser.*, 1153 (1), 012070.

[44] Sarangthem, V., Seo, B.Y., Yi, A., Lee, Y.J., Cheon, S.H., Kim, S.K., Singh, T.D., Lee, B.H., and Park, R.W., 2020, Effects of molecular weight and structural conformation of multivalent-based elastin-like polypeptides on tumor accumulation and tissue biodistribution, *Nanotheranostics*, 4 (2), 57–70.

[45] Sánchez-Pacheco, A.D., Hernández-Vergara, M., Jaime-Adán, E., Hernández-Ortega, S., and Valdés-Martínez, J., 2021, Schiff bases as possible hydrogen bond donors and acceptors, *J. Mol. Struct.*, 1234, 130136.

[46] Chen, H., Lu, Y., Shi, S., Zhang, Q., Cao, X., Sun, L., An, D., Zhang, X., Kong, X., and Liu, J., 2022, Design and development of a new glucagon-like peptide-1 receptor agonist to obtain high oral bioavailability, *Pharm. Res.*, 39 (8), 1891–1906.

[47] Gulati, P., Chadha, J., Harjai, K., and Singh, S., 2023, Targeting envelope proteins of poxviruses to repurpose phytochemicals against monkeypox: An *in silico* investigation, *Front. Microbiol.*, 13, 1073419.

[48] da Silva, M.M., Comin, M., Duarte, T.S., Foglio, M.A., De Carvalho, J.E., Vieira, M.D.C., and Nazari Formagio, A.S., 2015, Synthesis, antiproliferative activity and molecular properties predictions of galloyl derivatives, *Molecules*, 20 (4), 5360–5373.

[49] Roshdi, M., Mohamed, M.F.A., Beshr, E.A.M., Aziz, H.A., Gebril, S.M., Bräse, S., and Mohassab, A.M., 2025, Design, synthesis, in silico docking, multitarget bioevaluation and molecular dynamic simulation of novel pyrazolo[3,4-*d*]pyrimidinone derivatives as potential *in vitro* and *in vivo* anti-inflammatory agents, *Pharmaceuticals*, 18 (9), 1326.

[50] Tribudi, Y.A., Agustin, A.T., Setyaningtyas, D.E., and Gusmalawati, D., 2022, Bioactive compound profile and biological modeling reveals the potential roles of purified methanolic extract of sweet flag (*Acorus calamus* L.) in inhibiting the dengue virus (DENV) NS3 protease-helicase, *Indones. J. Chem.*, 22 (2), 331–341.

[51] Gokce, C., Altun, B., Kirit, E., Yavuz, H., Uyar, R., Celik, D., and Yilmazer, A., 2025, Unlocking the human blood-brain barrier (BBB) characteristics for the development of nano-delivery strategies for central nervous system therapies, *J. Drug Delivery Sci. Technol.*, 108, 106961.

[52] Sharma, P., and Shanavas, A., 2021, Natural derivatives with dual binding potential against SARS-CoV-2 main protease and human ACE2 possess low oral bioavailability: A brief computational analysis, *J. Biomol. Struct. Dyn.*, 39 (15), 5819–5830.

[53] Lee, M., Chan, C.W., Graham, S.C., Christopherson, R.I., Guss, J.M., and Maher, M.J., 2007, Structure of ligand-free and inhibitor complexes of dihydroorotase from *Escherichia coli*: Implications for loop movement in inhibitor design, *J. Mol. Biol.*, 370 (5), 812–825.

[54] Eakin, A.E., Green, O., Hales, N., Walkup, G.K., Bist, S., Singh, A., Mullen, G., Bryant, J., Embrey, K., Gao, N., Breeze, A., Timms, D., Andrews, B., Uria-Nickelsen, M., Demeritt, J., Loch, J.T., Hull, K., Blodgett, A., Illingworth, R.N., Prince, B., Boriack-Sjodin, P.A., Hauck, S., MacPherson, L.J., Ni, H., and Sherer, B., 2012, Pyrrolamide DNA gyrase inhibitors: Fragment-based nuclear magnetic resonance screening to identify antibacterial agents, *Antimicrob. Agents Chemother.*, 56 (3), 1240–1246.